DYNAMICS OF THE WING-TIP VORTEX IN THE NEAR FIELD OF A NACA0012 AIRFOIL*

C. del Pino, J.M. López-Alonso, L. Parras, and R. Fernandez-Feria
ETSI Industriales, University of Málaga, 29071 Málaga, Spain

1. Introduction.

Vortex meandering (or wandering) is a typical feature of wing-tip vortices that consists in a random fluctuation of its vortex centreline. This meandering of the vortex is quite significant a few chords downstream the wing, and was originally thought to be due to free stream turbulence [1], then to instabilities of the vortex core [2]. But, independently of the controversy about its origin [3], the quantitative characterization of the vortex wandering phenomenon is a subject of current research [4]-[6].

In this work we have undertaken a systematic visualization of the trailing vortex behind a NACA0012 airfoil at several distances near the wing tip for different angles of attack and different Reynolds numbers to characterize the structure of the vortex meandering phenomenon as well as its frequency, wavelength, and amplitude. The technique is similar to that used by Roy and Leweke [5], but we characterize the downstream evolution of these vortex meandering characteristics and, therefore, the dynamics of the wing-tip vortex in the near field.

2. Experimental setup.

For the experiments we used a closed circuit, horizontal water tunnel facility with a working section of 0.5 x 0.5 m^2 cross-section and 5m long installed in the Laboratory of Aero-Hydrodynamics of Vehicles at the University of Málaga. This long test section is made of *Plexiglas* to allow for optical visualizations, as well as for PIV and LDA quantitative measurements of the velocity field, all along its five meters long. The range of the free stream velocity (V) in the test section is 0-0.75m/s, which is achieved through two *ABB* centrifugal pumps of 18.5kW each. The maximum flow rate provided by each pump is about 350m^3/h. The flow rate is measured through a turbine FLS flow meter (model Flowx3), located downstream of the pump, which was previously calibrated through LDA and PIV measurements of the axial velocity field at several cross-sections. Flow uniformity is achieved by a series of honeycombs and screens sections in the settling chamber upstream the contraction located prior to the working section. The contraction ratio is 14:1 in section, which reduce the turbulence intensity in the test section by accelerating the mean flow. The mean turbulence intensity associated with the streamwise velocity is approximately 2%.

To generate a single wing-tip vortex we use a NACA0012 symmetric airfoil with a chord c=10cm, vertically mounted on the upper surface of the first sector of the channel working section, and with the rounded tip approximately centred in the test section (see Fig. 1). It is attached to this surface through a circular window especially designed to allow for the rotation of the wing into several positions, thus making possible the configuration of different angles of attack between the upstream flow and the wing. In addition, this window is provided with a connection between the system of controlled injection of dye and the wing, permitting flow visualizations in the wake behind the wing tip. The airfoil was machined in aluminium, and painted with a special black pigment to minimize corrosion by water.

For the visualization of the trailing vortex we used a green fluorescent dye (Rhodamin 6G) diluted in water. The dye is injected into the wake behind the wing from two small holes of diameter 0.5mm perforated along the wing and exiting at the wing tip. The fluorescent dye arrives to these holes from an injection system constituted by four deposits that contain the liquid dye, and a compressor with a valve system to control the dye injection flow rate. The vortex was illuminated normally to the mean flow with a laser sheet from a green (wavelength = 532nm) laser of 40mW (laser Z406; see Fig. 2).

To capture the vortex images we used a *Sony Handycam HDR-SR5* video-camera with a resolution of 1 Mpixel, 40 Gb of internal

memory, and a maximum shutter speed of 1/25s. This speed of 25 images captured per second was found to be well suited to characterize the meandering phenomena, whose main frequency was always well below 1Hz (see next section). Preliminary visualizations were made with a *Photron SA3* high-speed video-camera, but at the high speed of this camera one had to capture and process too many pictures to cover the time interval necessary to characterize with precision the meandering phenomenon (of the order of several minutes), and was discarded.

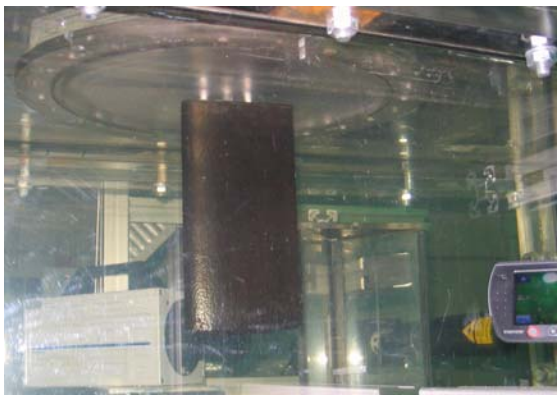

Figure 1: Photograph showing the wing and the two cameras used for the visualization.

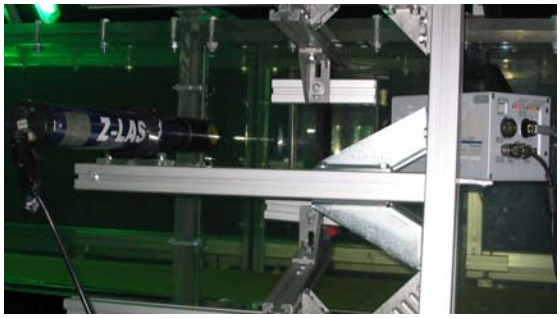

Figure 2: Photo of the visualization system with the laser source of 40 mW, the prismatic window attached to the test section of the tunnel, and the high-speed video-camera.

The cameras were mounted at an angle of 45º in relation to the test section, with the vortex illuminated by the laser sheet in the normal direction to the main flow at fixed distances downstream the trailing edge of the wing (see Fig. 2). Between the camera and the tunnel working section we installed prismatic windows to minimize refraction.

3. Results.

We have characterized the downstream evolution of the vortex meandering by processing the successive images captured at 5 different axial distances from the wing trailing edge, z/c=0.1, 1, 2, 3, and 4, where c is the wing chord, as a function of the upstream velocity (Reynolds number) and the angle of attack α. In particular, we have selected 5 different values of the tunnel flow rate, corresponding to five positions of the flow-meter frequency controller, and three different angles of attack, α = 6º, 9º, and 12º. This makes a total of 15 different configurations for each downstream location, i.e. 75 visualizations. Table 1 shows the mean values of the free stream velocity and Reynolds numbers associated to the five different flow rates used in the experiments.

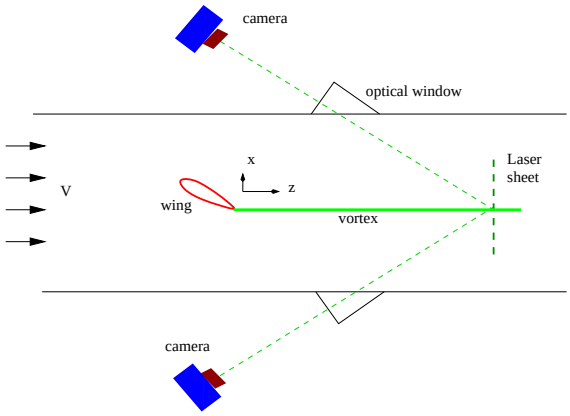

Figure 3: Sketch of the visualization system and coordinates.

Pot	Q(l/s)	V(cm/s)	Re	T(ºC)
5	63∓1.5	25.3∓0.6	22504∓533	15.9∓1
6	77∓2	30.8∓0.8	27441∓713	16∓1
7	90∓2	36.0∓0.8	32089∓713	16∓0.9
8	103∓2	41.3∓0.8	36871∓715	18.1∓0.9
9	117∓2	46.8∓0.8	41875∓717	16.2∓0.9

Table 1: Flow rate Q, mean velocity V=Q/A, where A is the area of the test section of the tunnel, and Reynolds number Re=Vc/ν, where c is the wing chord and ν the kinematic viscosity of water, corresponding to the 5 positions selected of the potentiometer (Pot) in the variable frequency drive of the flow meter. The errors in the Reynolds number take into account not only the fluctuations in the flow rate, but also those associated to the measured temperature through the kinematic viscosity, which is computed using an experimental relation given in White [7].

The main features of the wing-tip vortex sought from the image processing are the frequency and wavelength of the fluctuations (meandering), the distribution of the vortex centre positions, the angle of the main direction of these fluctuations, their amplitude, and the

spatial structure of the principal or most energetic oscillation modes. To these ends, we first make a preliminary transformation of the images to eliminate, or at least to reduce as much as possible, the deformation due to both the angle between the target plane and the camera, and to refraction. As can be seen in Fig. 4, this deformation is quite significant in spite of the use of an optical window attached to the tunnel wall. The figure shows one of the targets with a matrix of white concave 'dots' used for calibration of the PIV measurements, which is used here also for the calibration of the visualization images. The actual distance between the centres of the 'dots' is 2.5 mm. This target is positioned inside the working section of the water tunnel in the same cross-section plane of the laser sheet where the subsequent images of the vortex will be captured.

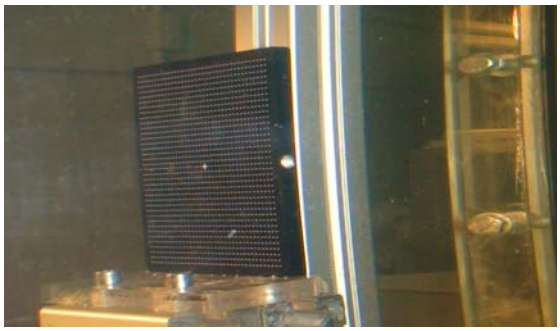

Figure 4: Image of the calibration target taken by the video-camera inside the test section of the tunnel.

The image of the target is transformed into a square by means of a bilinear transformation of a number of points. Since this transformation contains 12 unknown coefficients, we select at least 6 points of the target (x_i,y_i), and transform them into the calibrated, or transformed, points (X_i,Y_i). These six points are selected on a portion of the calibration target a little larger that the maximum size of the vortex core that will be visualized. It turns out that the best calibration for our objectives is obtained by selecting the central section of the calibration target with a size of about 12 x12 white 'dots', i.e. of about 9 cm^2. Figure 5 shows this central portion of the calibration target both as captured by the camera and after the transformation. The resulting transformation is then applied to all the images of the trailing vortex taken on the same plane thus calibrated. Figure 6 shows an example of how the core of the vortex, whose fluorescent dye is illuminated by the green laser sheet, is transformed from the distorted image captured by the camera into its actual shape in the normal plane to the vortex axis. Since this calibration process is quite lengthy in time, because one has to open the water tunnel to extract the calibration target and then run the tunnel again for visualizations after each calibration, we optimize the overall visualization process by capturing all the images needed in a given section z/c downstream the wing, for all the flow rates and angles of attack considered, and then move to the next section.

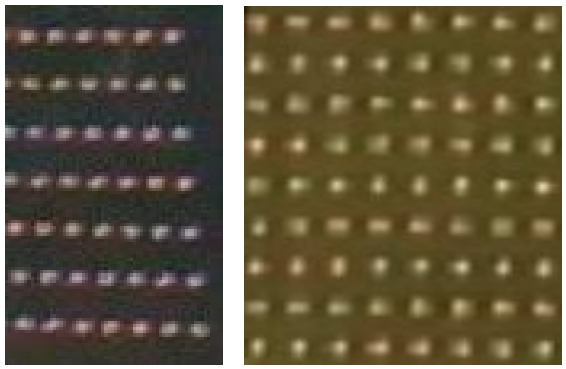

Figure 5: Images of the central portion of the calibration target before (left) and after (right) the transformation.

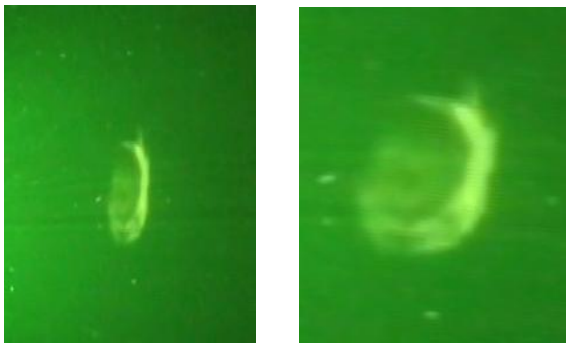

Figure 6: Cross-sectional images of the vortex illuminated with the laser sheet before (left) and after (right) the transformation resulting from the calibration (the scales of the images are not the same).

For each of the values of the parameters Re, α, and of the distance z/c selected, with a total of 5x3x5 = 75 different configurations, we capture about 13,000 images with the *Sony HDR-SR5* video-camera at a rate of 25 images per second, which therefore takes more than 8 minutes for configuration. This time interval is large enough to compute mean values of the vortex meandering (as we shall see below, the meandering frequency is typically less than 1 Hz). The main problem, however, is not time, but the huge amount of memory needed to store

all these images, which are duplicated because we save both the original and the calibrated images.

3.1 Statistical analysis of the vortex centre position.

The first information that we extract from the calibrated images of the vortices captured for a given set of parameters is the distribution of the positions of their centre or vortex axis. This is done by previously applying a *threshold segmentation technique* to these transformed images. Basically, this technique consists on transforming a grey scale picture into a binary black and white one by using a given brightness threshold, in such a way that the pixels with brightness below that threshold are converted to black, and those with brightness above it are set white. The main problem is to select the appropriate threshold, and also to decide whether a fixed or a variable threshold is more convenient. In the present case, where there exists a significant contrast between the fluorescent dye illuminated by the laser, which is concentrated in the vortex core, and the rest of the picture, which is rather dark (see Fig. 6), a *fixed* threshold works well, which is in addition relatively easy to select by trial and error: different thresholds in a certain range yield the same segmented image. An example of the application of this technique to the transformed image of a vortex core in given in Fig. 7.

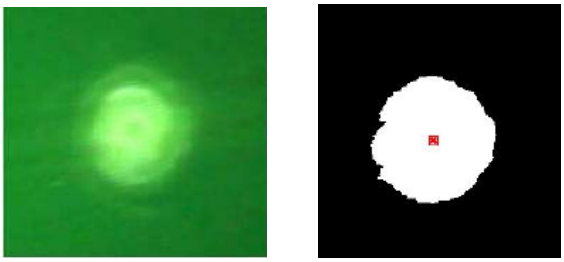

Figure 7: Calibrated image of the vortex core (left) and the resulting image after applying thresholding segmentation with a fixed threshold (right). Also shown is the computed centroid of the segmented image.

Once the vortex core is segregated from the rest of the image, the centre of the vortex is obtained by computing the centroid ('centre of mass') of the largest 'white' region of the segmented (binary) image using a *Matlab* code (see Fig. 7). This approximation is based on the reasonable assumption that the dye distribution is well centred on the vortex axis, which depends on an adequate positioning of the dye injection holes on the wing. We compute this centroid for several threshold values and check the consistency of the method by finding an interval of threshold values that yields the same centroid. In fact, this is the way in which the threshold intensities are selected by trial and error for each image. It turns out that practically the same threshold value can be used for all the images considered here.

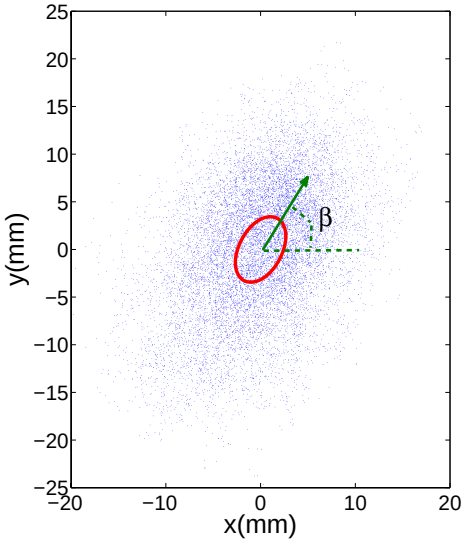

Figure 8: Distributions of the vortex centre positions for Re=41875, α=12º, and z/c=4. Coordinates are centred on the mean position. Each blue dot represents the centre position (x_c,y_c) in one visualization frame. The red curve is an ellipse of radii a_M and a_m, whose major axis forms an angle β with the horizontal.

The operation is repeated for every image captured by the video-camera in a run (about 13,000 frames) for a given flow rate, angle of attack, and distance to the wing, so that a statistical treatment of the transverse position of the vortex centre can be made, and thus characterize several aspects of the vortex meandering phenomenon [5]. Figure 8 shows an example of the vortex centre positions (x_c,y_c) obtained with the above technique from the about 13,000 images captured at a rate of 25 Hz for a given set of parameters. The origin of coordinates is set at the mean value of the vortex centre positions.

To characterize the distribution of the transverse position of the vortex centre we compute the eigenvalues a_M^2 and a_m^2 of the covariance matrix of the vectors x_c and y_c. For $a_M^2 > a_m^2$, the two corresponding eigenvectors

$\mathbf{v}_M$ and $\mathbf{v}_m$ are the directions in which the statistical dispersion is maximal and minimal, respectively, the eigenvalues being the corresponding variances in both directions. a_M and a_m can be considered as dispersion radii in the $\mathbf{v}_M$ and $\mathbf{v}_m$ directions.

An angle β can be defined between the horizontal direction and the direction of the major axis $\mathbf{v}_M$ of the vortex position distribution. A convenient way to illustrate these quantities is by plotting the ellipse of radii a_M and a_m aligned in the the principal directions $\mathbf{v}_M$ and $\mathbf{v}_m$ (see Fig. 8). We have corroborated that the error in the computed a_M, a_m, and β with 13,000 frames is less than 1%, by using an increasing number of frames from 2,000 on.

Figures 9-10 show the downstream evolution of the mean statistical properties of the vortex; i.e., a_M, a_m, and β plotted against z/c for given angles of attack and for the different Reynolds numbers considered. These figures show that the influence of the Reynolds number on these mean quantities is quite small, except for the angle β close to the wing tip, where the vortex is still building up. For α=9º and 12º it is observed that the amplitude of the vortex, characterized by the eigenvalues a_M^2 and a_m^2 (Fig. 9), fluctuates up to z/c=2, with a local maximum at z/c≃1 and a local minimum at z/c≃2, and then increases steadily. This behaviour indicates that the rollup of the vortex sheet created by the lift of the wing develops in a region between the wing tip and two chord downstream, approximately, until the vortex is formed at z/c≃2, whose amplitude is still growing at z/c=4. For the smallest angle of attack considered, α= 6º, the region of vortex formation extends further downstream, until z/c≃3, with no appreciable local minimum of the vortex amplitude in the building up region. The angle β (Fig. 10), however, shows that the region of vortex formation extends in fact up to z/c≃3 for the three angles of attack, with marked fluctuations in β up to this axial station. This discrepancy is probably due to the discrete axial locations where visualizations are captured. Downstream z/c=3, the angle β does not depends practically on the Reynolds number and its value decreases slowly with z, indicating again that the downstream asymptote has not been reached yet at z/c=4, but that it will be close to 70º.

In summary, the amplitude and the angle of the vortex fluctuations characterized from images captured at several axial locations downstream the wing show that a vortex is formed between the wing tip and 2 or 3 chords downstream, depending on the angle of attack. In this region the flow must be very complex due to the interaction of the wing tip boundary layer and the incipient vortex. After this region of vortex formation, the meandering amplitude grows and its angle decreases until, eventually, they reach asymptotic values downstream, which at z/c=4 have not been reached yet for the Reynolds numbers and the angles of attack considered.

3.2 Vortex perturbation structure.

The above analysis of the visualization images provides a characterization of the vortex centre fluctuations with the distance to the wing, the Reynolds number, and the angle of attack. But these images can also be used to characterize the precise nature of the vortex perturbation with respect to the axisymmetric reference flow, determining the spatial structure of the most energetic non-axisymmetric modes. Then, using the first most energetic mode, we can characterize the frequency and wavelength of the meandering of the vortex.

An efficient way to extract a set of modes characterizing the perturbation of a given base flow is to perform a singular value decomposition, or Proper Orthogonal Decomposition (POD), which is a powerful and elegant method of data analysis aimed at obtaining low-dimensional approximate descriptions of high-dimensional processes, and which has been extensively used to characterize turbulent flows [8]. In the case of a vortex, as in turbulent flows, it is appropriate to use the vorticity distribution for this type of analysis. But we follow here Roy and Leweke [5] and use the light intensity field of the dye visualization frames, instead of the vorticity field, to perform the POD analysis of the present wing-tip vortices. Contrary to PIV measurements, dye visualization only requires a single frame at a time, allowing much longer acquisition periods for a given computer memory, and these authors demonstrated that the results are practically identical to those obtained from the vorticity distribution computed from quantitative PIV measurements of the vortex.

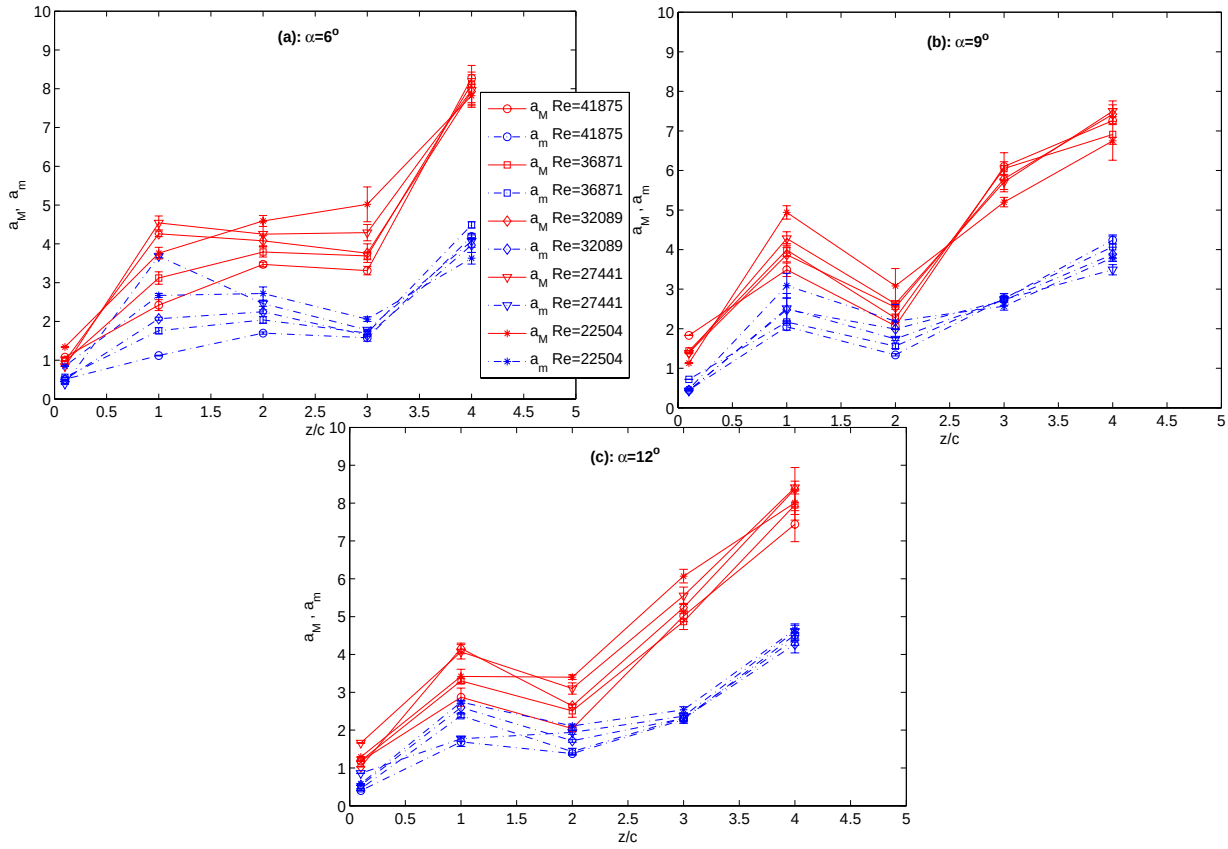

Figure 9: Downstream evolution with z/c of the amplitudes a_M (continuous lines) and a_m (dashed-and-dotted lines), given in *mm*, for the different Reynolds numbers considered (as indicated in the legend), and for the three values of the angle of attack considered, as indicated in each sub-figure (a) to (c).

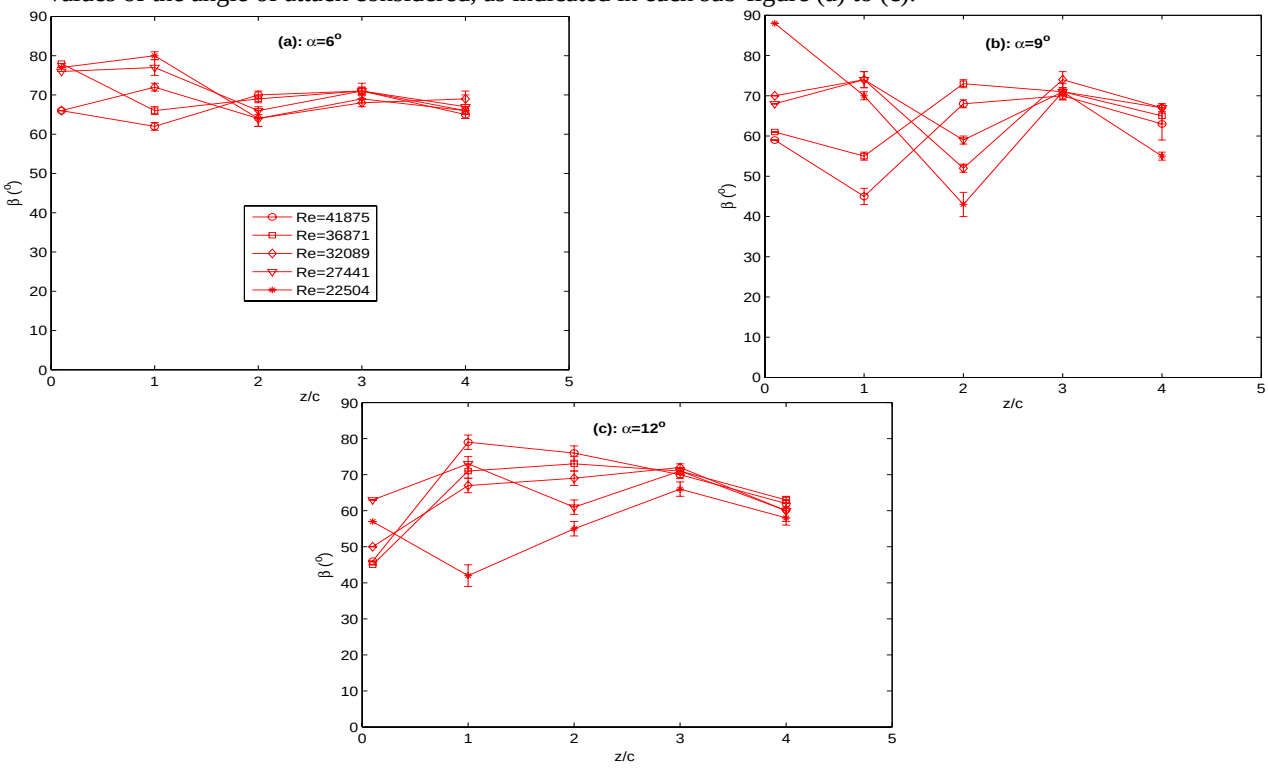

Figure 10: Evolution with z/c of the vortex ellipse angle β, for the different Reynolds numbers considered (as indicated in the legend), and for the three values of α considered, as indicated in each sub-figure (a) to (c).

To illustrate the method, Fig. 11 shows the results for the case α=9º, Re=36871 and z/c=4 [we shall use the shorthand (9.8.4) to cite the different configurations, where the second digit refers to the Reynolds number according to the Pot. position in Table 1]. These results are qualitatively similar to those reported by Roy and Leweke [5] for z/c=11.2 and for higher Reynolds numbers than the ones considered here. The first sub-figure (upper-left) shows the square root of the seven largest eigenvalues, which correspond to the relative amplifications of the seven most energetic modes of the vortex. The spatial structure of the five most energetic modes are shown in the next five sub-figures, as indicated. The axes of these last sub-figures represent pixels. The matrix A, whose singular value decomposition is made, is a huge matrix build up with the successive images captured for a given case. Each column of this matrix A contains the intensity of light corresponding to every pixel of the image captured in an instant of time. Thus, if the number of selected pixels for image processing is $np=np_x \times np_y$, and the number of captured images in a given case is ni, the dimension of matrix A is np x ni (typically of the order of $10^4 \times 10^4$ for the 13,000 frames captured). To perform the singular value decomposition of such a huge matrix we use the Arnoldi iteration method (see, e.g., [9]) to search only for the largest 7 eigenvalues and their corresponding eigenvectors, corresponding to the seven most amplified modes, thus reducing to a great extent the huge amount of computer memory, and of computation time, that would be needed to obtain all the eigenvalues and eigenvectors of A. With this process, the original image is decomposed in seven images, each one corresponding to the first seven eigenvectors U_i, i=1,...,7, of A, whose amplification or weight in the original image is proportional to the square root of the corresponding eigenvalue s_i.

The first mode in Fig. 11, whose amplitude is almost two orders of magnitude larger than the second one, corresponds obviously to the axisymmetric base (vortex) flow. The next two most amplified modes correspond to a non-axisymmetric perturbation with azimuthal wave number n=1, representing the main lateral displacement of the vortex due to the meandering phenomenon. The principal directions of these two modes form an angle of 90º between them, so that they constitute the two independent modes with n=1, whose superposition accounts for the lateral displacements of the vortex in any direction (note that the amplitude of these two modes is practically the same). In addition, the principal direction of the second most amplified mode is found to form an angle that is practically coincident with the angle β obtained from the image analysis of the preceding sub-section for this case. All this support that these most energetic modes with n=1 characterize the vortex meandering.

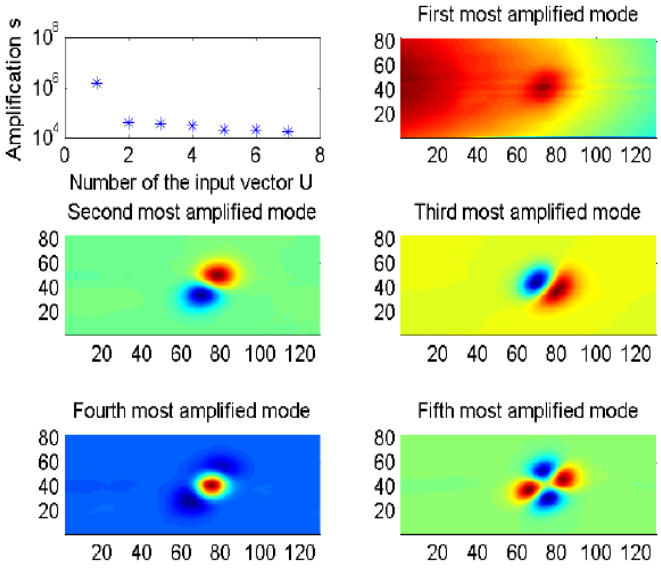

Figure 11: Perturbation characterization through POD analysis for the case (9.8.4).

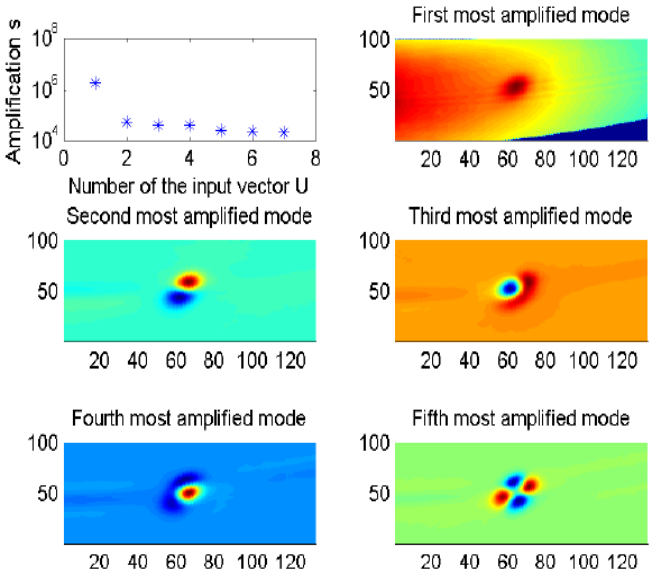

Figure 12: Perturbation characterization through POD analysis for the case (12.6.3).

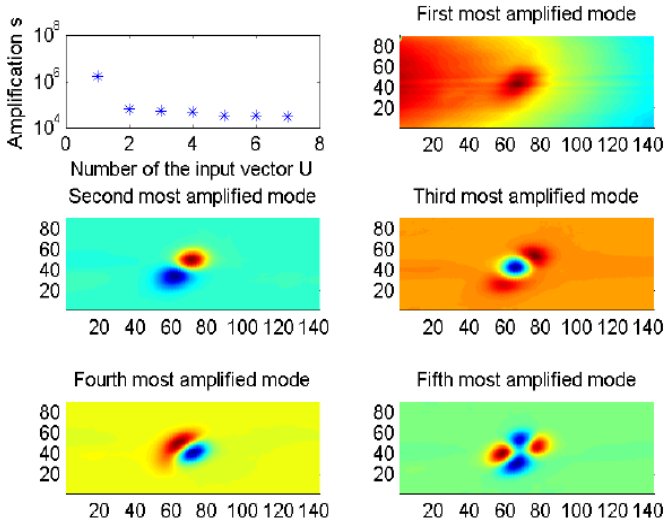

Figure 13: Perturbation characterization through POD analysis for the case (12.7.4).

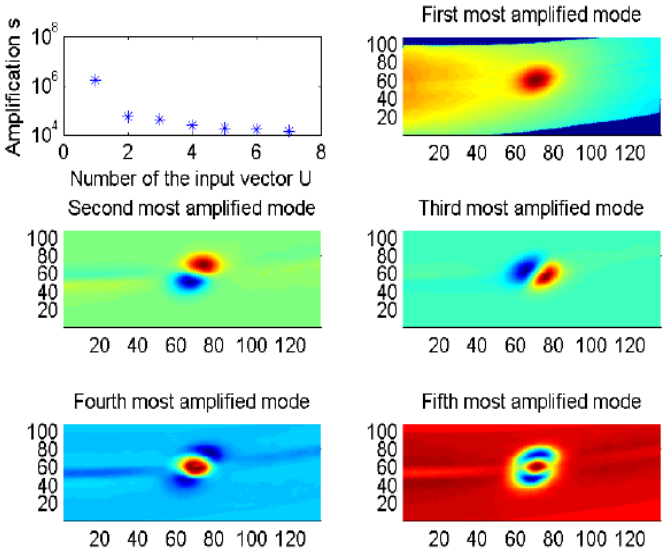

Figure 14: Perturbation characterization through POD analysis for the case (6.7.3).

The next two modes, which are the last ones shown at the bottom of Fig. 11, have an azimuthal wave number n=2, and represent elliptical deformations of the axisymmetric vortex. The amplitudes of the next modes (not shown) with azimuthal wave numbers n=3,4,..., are much smaller, so that they are almost irrelevant in the structure of the perturbation of the vortex, and are not considered here. Similar structure to that depicted in Fig. 11 is found for all the cases considered with z/c=4, except for (12.7.4), (9.6.4), (9.5.4), (6.6.4), and (6.5.4), and with z/c=3 with α=12º, and 9º, except for low Reynolds numbers, i.e. for (12.6.3), (12.5.3), (9.6.3), and (9.5.3).

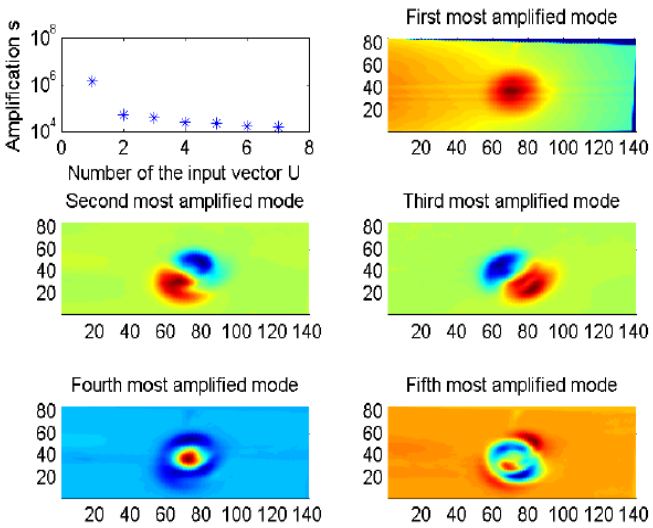

Figure 15: Perturbation characterization through POD analysis for the case (12.7.1).

A slight deviation with respect to the behaviour shown above occurs at the lowest Reynolds numbers considered for z/c=3, and 4, and it is shown in Fig. 12 for the case (12.6.3), appearing also for the cases (9.5.4), (9.6.4), (6.5.4), (6.6.4), (12.5.3), (9.5.3), and (9.6.3). The modes 3 and 4 considered above have disappeared, giving rise to two opposite modes with a structure similar to that of the fourth mode in Fig. 11.

It is convenient to note that this particular perturbation structure is not reached by decreasing the Reynolds number when α=12º and z is equal to four chords, but one obtain the main structure far from the wing given in Fig. 11, as mentioned above. But for these α and z, the structure is different when the Reynolds number is higher, as shown in Fig. 13 for the case (12.7.4). It is observed that the original third and fourth modes appearing in Fig. 11 are interchanged, which means that one of the modes with azimuthal wave number n=1, and which represents a lateral displacement of the vortex, is less energetic in this case than one of the modes with n=2, representing an elliptic compression of the vortex. This mode interchange appears also in the cases (9.8.2) and (6.8.2).

All the cases with α=6º and z/c=3, together with all the cases for z/c=2, share the peculiarity that the fifth mode is different to that appearing in the first configuration considered, with a structure similar to the fourth mode, as shown in Fig. 14 for the case

(6.7.3). It is interesting to note that for α=6º, the perturbation structures for z/c=3 and z/c=2 are qualitatively similar, a behaviour that is also observed in relation to the amplitudes a_M and a_m, and which may be related, as it was commented on in the preceding section, to the longer distance needed for the single vortex formation when the wing angle of attack is smaller.

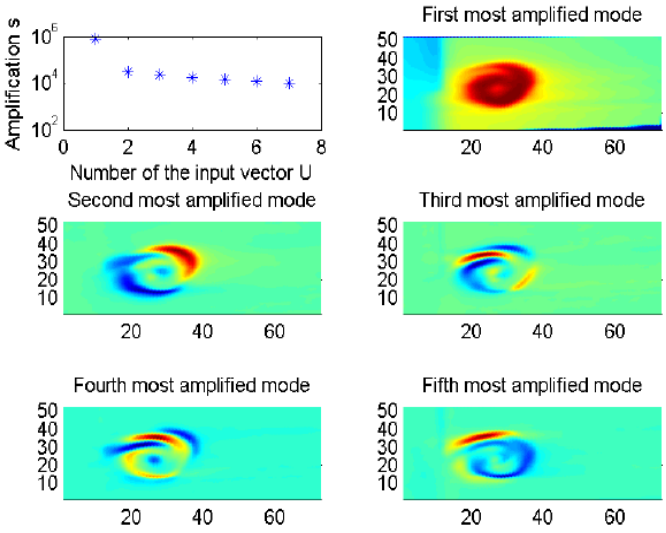

Figure 16: Perturbation characterization through POD analysis for the case (12.8.01).

To finish the description of the spatial structures of the vortex perturbation through POD analysis of the visualization images, Figs. 15 and 16 show the results obtained for shorter distances to the wing, where the vortex is still building up. One may distinguish two qualitatively different behaviours. The first one for z/c=1 and the flow rates corresponding to the Pot. positions 7,8, and 9, shown in Fig. 15 for the case (12.7.1), and the second one for the lowest Reynolds numbers (Pot. positions 5 and 6) when z/c=1, and all the cases considered for z/c=0.1, shown in Fig. 16 for the case (12.8.0.1). In the first case (Fig. 15), the first three azimuthal modes are similar to the first case considered (Fig. 11), but the fourth and fifth modes are quite different, showing a rotation of the vortex axis in the process of its formation. In the second case (Fig. 16), all the azimuthal modes are qualitatively different to those depicted in Fig. 11, clearly showing that the vortex is not yet formed (note the spiral structure), since they do not describe a clear lateral displacement corresponding to vortex meandering as observed for larger distances to the wing.

3.3. Meandering frequency and wavelength.
Once the spatial structure of the perturbation is characterized, we proceed to quantify the displacement frequency of the vortex centre (meandering frequency) by using the most energetic perturbation mode with azimuthal wave number n=1 (mode 2). To this end, we use the time-dependent projection on mode 2 of the 13,000 images captured in each case. To check the accuracy of the results, the same process has been repeated for different number of frames, with practically the same results when using more than 1,250 frames (50 s).

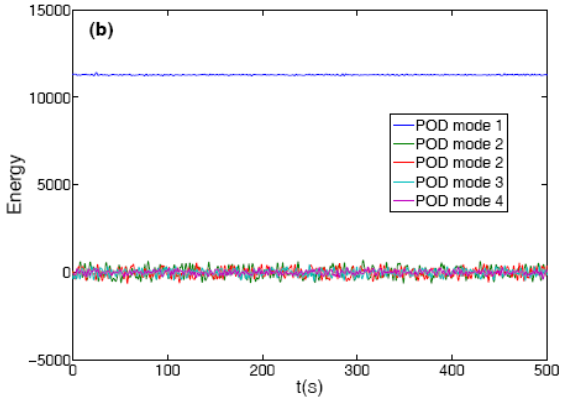

Figure 17: Energy of the first five modes vs. time for the case (12.9.4), after applying a high frequency filter.

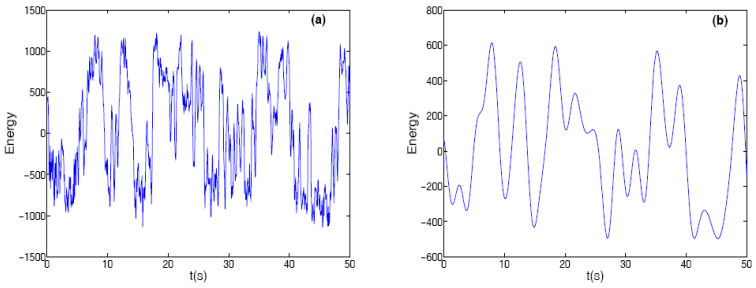

Figure 18: Energy of the second mode vs. time as computed form the images (a), and after applying a high frequency filter (b).

The time-dependent projection on each mode yields the relative energy as a function of time associated to that mode, as seen in Fig. 17 for the case (12.9.4). As expected, the projection is centred on zero for all the perturbation modes (2 to 5 in the figure). The figure shows the filtered results, i.e. eliminating very high frequency noise. Mode 1, which is obviously the most energetic, has no oscillations since it represents the axisymmetric base flow. From the oscillations of the remaining modes (centred on zero) we may infer the corresponding frequency spectra by using, for instance, a Fast Fourier Transform (FFT) of the

filtered signal (we use a standard *Matlab* subroutine to perform these FFT).

Figure 18 shows the energy of mode 2, for the same case of Fig. 17, plotted in the time interval $0 \leqslant t \leqslant 50$ s, both as they result directly from the projection of matrix A, and the filtered results. The results of the FFT applied to the filtered energy of this most energetic perturbation are given in Fig. 19, where the power spectral density P is plotted against the frequency f (in Hz). As the characteristic frequency f_p of the perturbation (characterized here by mode 2) we use that with highest spectral density. In this case it is found that $f_p \backsimeq$ 0.1385 Hz (see inset in Fig. 19).

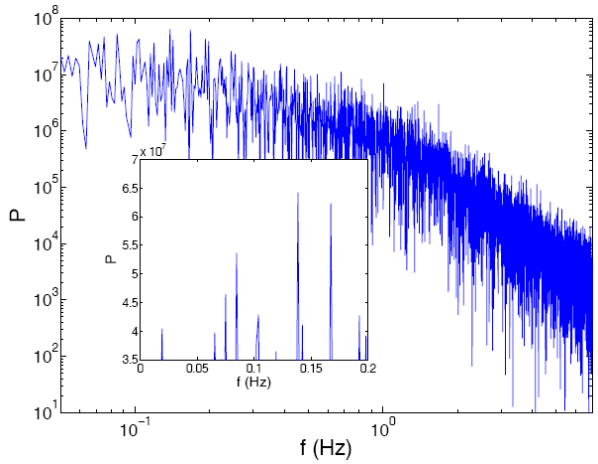

Figure 19: Power spectra density P resulting from the application of the FFT to the temporal energy distribution plotted in Fig. 18(b).

The characteristic frequencies obtained for all the other cases considered here are of the same order of magnitude, remaining always smaller than 0.2 Hz, approximately (see below). Since these meandering main frequencies are significantly smaller than those obtained in other investigations on wing-tip vortices [5-6], we have checked the results by computing the main meandering frequency from an alternative method, consisting on applying the FFT to the temporal evolution of the position of the center of the vortex obtained from the visualizations described in 3.1. Figure 20 shows the results for the same case (12.9.4), whose distribution of the vortex center positions is plotted in Fig. 8. The main frequency obtained from this distribution of the vortex axis position in time is almost identical to the one obtained above with the most energetic perturbation 2: now we find from Fig. 20 that $f_p \backsimeq$ 0.1384 Hz. The same occurs for all the cases considered.

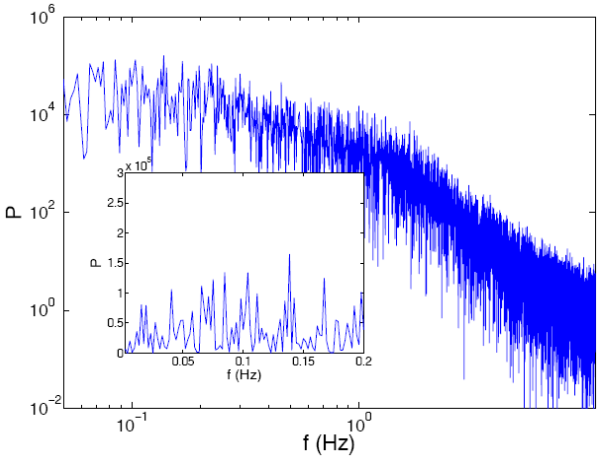

Figure 20: Power spectra density P resulting from the application of the FFT to the temporal evolution of the vortex centre in the case (12.9.4).

The main meandering frequency has been thus obtained for all the cases considered in this work. The results are summarized in Fig. 21, where this main frequency is plotted against z/c for given angles of attack α and for the different Reynolds numbers considered, thus showing the downstream evolution of the meandering frequencies for the different cases. It is observed that the streamwise fluctuations of the meandering frequency are larger than for their amplitude or their angle β (compare with Figs. 9-10), and they are not confined in a vortex formation region of just a few wing chords. This may be due to the fact that the vortex wandering is probably characterized by more that just a single frequency f_p, as shown by the spectra in Figs. 19-20. But the most significant result is the very low meandering frequencies found here, typically of the order of 10^{-1} Hz, and less than 0.2 Hz in all the cases considered. This does not agree with previous experimental results on vortex meandering, where the measured frequency was about 1 Hz or just a bit smaller [5-6]. Most of these previous results are computed at larger distances to the wing-tip than in the present visualizations, and for larger Reynolds numbers (z/c=11.2 and Re about 10^6 in [5]), but it does not seem plausible that the present frequencies will change so much from z/c=4 to z/c of the order of tens, and the dependence with the Reynolds number found here is not very significative.

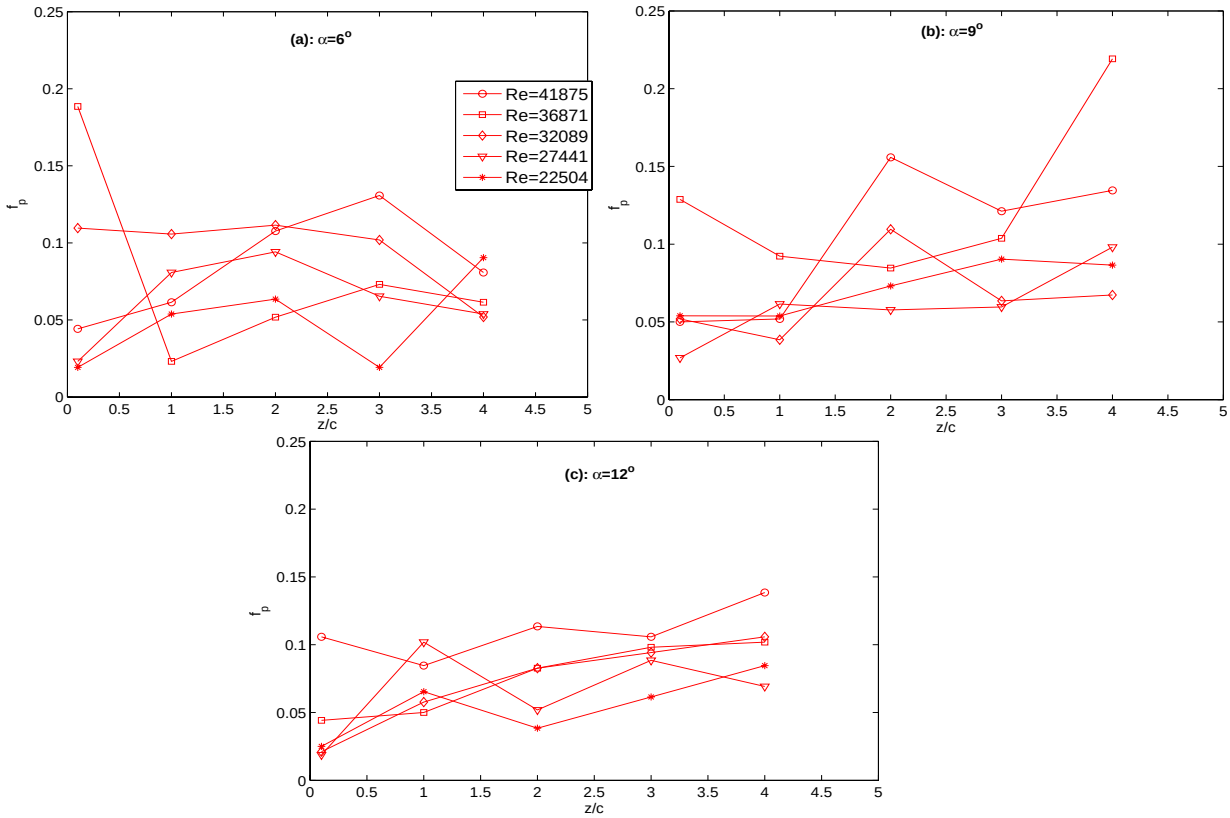

Figure 21: Evolution with z/c of the main frequency f_p (in Hz), for the different Reynolds numbers considered (as indicated in the legend), and for the three values of the angle of attack considered, as indicated in each sub-figure (a) to (c).

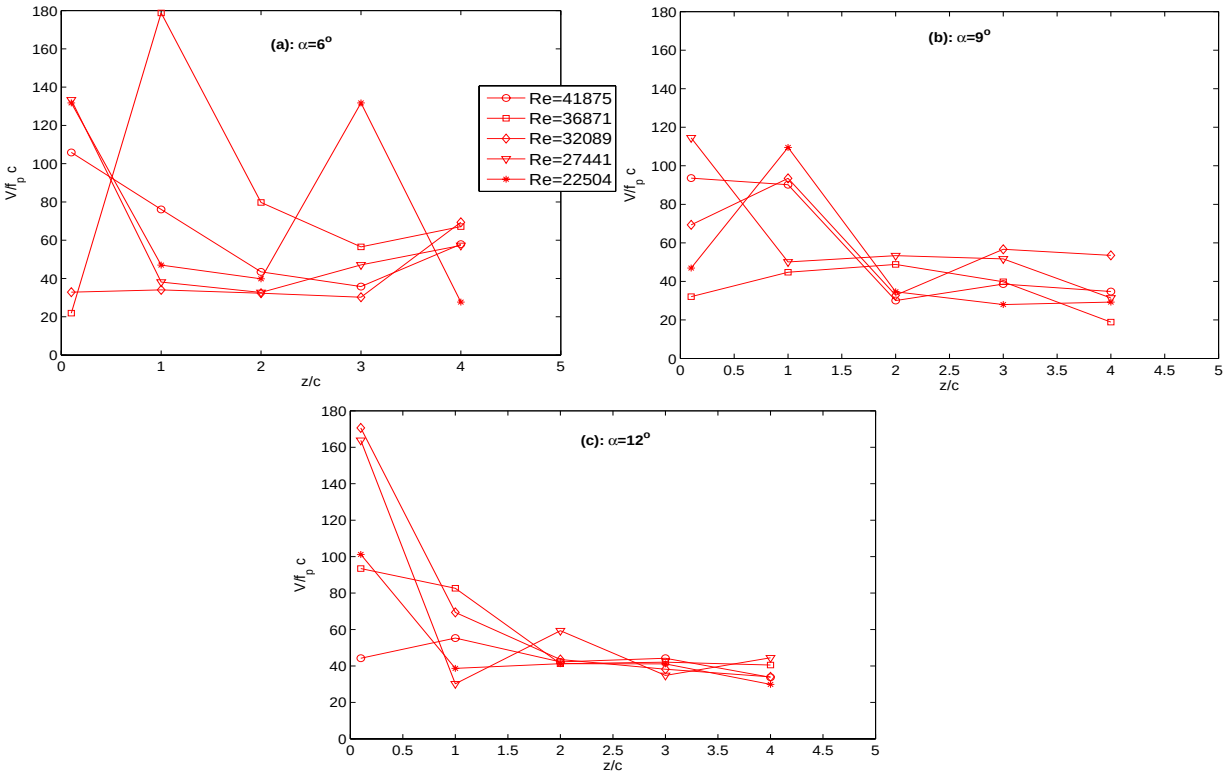

Figure 22: Evolution with z/c of the main non-dimensional wavelength $V/(f_p\ c)$, for the different Reynolds numbers considered (as indicated in the legend), and for the three values of the angle of attack considered, as indicated in each sub-figure (a) to (c).

To perform a better comparison with the recent results by Bailey and Tavoularis [6], Fig. 22 shows the non-dimensional wavelength of the meandering phenomena associated to the frequency f_p, that is $V/(f_p c)$, for the same cases considered in Fig. 21. The vortex meandering evolution shown in this figure is in qualitative agreement with that in Figs. 9-10, with a vortex formation region of about 2 or 3 chords, except for the lowest value of the angle of attack considered. But the values are again more than one order of magnitude larger (in this case) than those reported in the previous work (e.g., Fig. 13 in Ref. [6]).

4. Conclusions.

We have characterized the meandering phenomenon of a wing-tip vortex in the near field behind a NACA 0012 airfoil by quantitative analysis of the images taken at different cross sections (z/c =0.1, 1, 2, 3, and 4) downstream of the wing trailing edge. We have processed 13,000 images taken at a rate of 25 frames per second at each downstream location, for three different angles of attack (6º, 9º, and 12º), and for five different Reynolds numbers between about 20,000 and 40,000. In particular, we have characterized the downstream distribution of the vortex centre, and the amplitude and angle of their wandering oscillations. We find that the vortex formation takes place in a distance behind the wing between 2 and 3 chords, depending on the angle of attack, and that the results are almost independent of the Reynolds number for the range of Reynolds numbers considered. We have also characterized the structure of the wandering phenomenon by means of a POD analysis of the images, finding that the most energetic mode of the perturbations of the original axisymmetric vortex has an azimuthal wavenumber n=1, with an angle that coincides with that obtained from the distributions of the vortex centre, so that this perturbation characterizes the meandering phenomenon.

One of the main conclusions of the present work is that the main frequency of this most energetic, or dominant, perturbation mode of the vortex coincides with the main frequency obtained from the analysis of the distribution of the vortex centre positions and, therefore, characterizes the vortex meandering frequency. But the values obtained in the present work, of the order of 10^{-1} Hz, are almost one order of magnitude smaller than in previously related works [4-5]. Corroborating this discrepancy, the non-dimensional wavelengths computed from these frequencies are about one order of magnitude larger than those reported in another recent work on vortex meandering [6]. We have to explore larger downstream distances to the wing-tip (up to tens of chords), and higher Reynolds numbers to see whether these discrepancies tend to disappear as z/c and Re increase, or they persist. This is a work in progress.

References.

[1] G.R. Baker, S. J. Barker, K. K. Bofah, and P. G. Saffman. Laser anemometer measurements of trailing vortices in water. *J. Fluid Mech.*, 65:325, 1974.

[2] S. I. Green and A. J. Acosta. Unsteady flow in trailing vortices. *J. Fluid Mech.*, 227:107–134, 1991.

[3] D. Fabre, J. Fontane, P. Brancher, S. Le Dizès, C. Roy, T. Leweke, R. Fernandez-Feria, L. Parras, and C. del Pino. Syntesis on vortex meandering. Technical Report D.1.1.1, STREP project no. AST4-CT-2005-012238, Fundamental research on aircraft wake phenomena (FAR-Wake), 2008.

[4] W. J. Devenport, M. C. Rife, S. I. Liapis, and G. J. Follin. The structure and development of a wing-tip vortex. *J. Fluid Mech.*, 312:67–106, 1996.

[5] C. Roy and T. Leweke. Experiments on vortex meandering. Technical Report TR 1.1.1-4 STREP project no. AST4-CT-2005-012238, Fundamental research on aircraft wake phenomena (FAR-Wake), CNRS-IRPHE, 2008.

[6] S. C. C. Bailey and S. Tavoularis. Measurements of the velocity field of a wing-tip vortex, wandering in grid turb-ulence. *J. Fluid Mech.*, 601:281–315, 2008.

[7] F.M. White. *Fluid mechanics*. McGraw-Hill, New York, 2005 (Fifth ed.).

[8] G. Berkooz, P. Holmes, and Lumley J. L. The proper orthogonal decomposition in the analysis of turbulent flows. *Annu. Rev. Fluid Mech.*, 25:539–575, 1993.

[9] Y. Saad. *Iterative methods for sparse linear systems*. SIAM, Philadelphia, second edition, 2003.

*This work has been supported by the Junta de Andalucía (Spain) Grant No. P05-TEP-170.